Cement and Concrete Composites 143 (2023) 105230

Contents lists available at ScienceDirect

Cement and Concrete Composites

journal homepage: www.elsevier.com/locate/cemconcomp

Characterisation of alkali-activated stainless steel slag and blast-furnace slag cements

Saeid Ghorbani [a,1], Laura Stefanini [b,1], Yubo Sun [a], Brant Walkley [c], John L. Provis [b,*], Geert De Schutter [a], Stijn Matthys [a]

[a] Magnel-Vandepitte Laboratory, Department of Structural Engineering and Building Materials, Faculty of Engineering and Architecture, Ghent University, Technologiepark-Zwijnaarde 60, 9052, Belgium
[b] Department of Materials Science & Engineering, University of Sheffield, Sir Robert Hadfield Building, Mappin Street, Sheffield, S1 3JD, United Kingdom
[c] Department of Chemical & Biological Engineering, University of Sheffield, Sir Robert Hadfield Building, Mappin Street, Sheffield, S1 3JD, United Kingdom

ARTICLE INFO

Keywords:
Alkali activated materials
Ground granulated blast furnace slag
Stainless steel slag
Characterisation
Microstructural analysis
Leaching

ABSTRACT

Rapid global industrial growth is causing an increase in the generation of large-scale by-products and waste materials, which can be recycled in the construction industry to decrease both the environmental impact of the sector and the impact of these waste materials, to ultimately contribute to the circular economy. In the current study, electric arc furnace stainless steel slag (EAFSS) as a potential precursor in the production of alkali activated materials (AAMs) is investigated, along and alternatively to the use of ground granulated blast-furnace slag (GGBFS). Five blended mixtures with different levels (0, 25, 50, 75 and 100 wt %) of EAFSS to replace GGBFS are activated with an alkaline silicate solution. Partially replacing GGBFS with EAFSS prolongs the dormant period in reaction and reduces the overall heat release of the paste mixtures. This results in a positive effect on fresh-state properties, increasing and prolonging workability and mixture setting times. A general decrease in strength is seen with EAFSS inclusion, although satisfactory compressive and flexural strength values of more than 85 and 9 MPa, respectively, were obtained at 28 days with up to 50% replacement of GGBFS by EAFSS. Most of the crystalline phases present within EAFSS do not participate notably in alkali-activation, other than merwinite which slowly dissolves and reacts to form a weak binder phase. The chromium present in the EAFSS is contained in a stable spinel phase; this element does not appear to be mobile in leaching tests.

1. Introduction

Alkali activation technology is now a serious pathway to significantly reduce carbon emissions of the construction sector [1,2], and involves mixing an activator and a solid precursor together to form a hardened cementitious system. The requirements for the precursor materials are different and less stringent than in conventional cements [3,4]. The versatility of alkali activation technology stems from the diversity of precursor materials that can be alkali activated, the most impactful of which with regard to sustainability and circular economy aspects include slags that are generated as by-products from large scale metallurgical processes, including but not limited to blast furnaces [5–8].

Alkali activation may also provide a fundamental route for the immobilisation of heavy metal-containing wastes originating from metallurgical processes [9,10], including stainless steel production. Stainless steel slags are generated in considerable volumes, up to about 300–400 kg of slags for each tonne of stainless steel produced [11,12], and are classified according to which type of furnace generates them, because this influences the properties, composition, and mineralogy of the slags. Cooling conditions and post-processing are also important in defining the characteristics of slags in alkali-activation. Traditional methods of steelmaking use a blast-furnace to obtain molten pig iron from iron ore. Ground granulated blast furnace slag (GGBFS) is the comminuted product of rapidly quenched blast-furnace slag separated from molten pig iron. GGBFS is one of the most common supplementary cementitious materials (SCMs) due to its consistent chemical composition and predominantly amorphous structure. Molten pig iron is then transformed into crude steel in a basic oxygen furnace, the by-product of which is basic oxygen furnace slag (BOFS). BOFS has a more variable

* Corresponding author.
E-mail address: j.provis@sheffield.ac.uk (J.L. Provis).
[1] these authors contributed equally to the work.

https://doi.org/10.1016/j.cemconcomp.2023.105230
Received 26 December 2022; Received in revised form 1 June 2023; Accepted 1 August 2023
Available online 2 August 2023

Table 1
Chemical composition of solid precursors detected by X-ray fluorescence spectroscopy.

Solid precursor	Chemical composition (%)									
	SiO_2	CaO	Al_2O_3	Fe_2O_3	MgO	SO_3	K_2O	MnO	Cr_2O_3	Others
GGBFS	31.1	40.9	13.7	0.4	9.2	2.3	0.7	0.3	–	1.4
EAFSS	28.0	44.2	6.3	2.0	4.4	0.5	0.1	2.6	9.9	2.0

chemical composition depending on the specific steelmaking plant, predominantly consisting of stable crystalline phases that lower its overall reactivity in alkali-activation compared to GGBFS. BOFS is primarily used as a cement aggregate. Alternative steel production from scrap sources using an electric arc furnace produces electric arc furnace stainless steel slag (EAFSS) that has similar characteristics are BOFS.

The increasing demand for GGBFS as a SCM in blends with Portland cement has provided further impetus to explore other waste products, specifically from the steelmaking industry, as potential AAMs [11]. The usage of various waste products from each step of the steelmaking process of different alloy types allows for further increases in sustainability and scientific research in both steelmaking and construction industries. However, the inconsistency in waste compositions [13,14] and the presence of heavy metals are major limitations to the valorisation of steel slags; the leaching of toxic chromium compounds contained in stainless steel slags has been noted as being of particular concern [15–17]. Global stainless steel slag production is reported to have been around 52 million tonnes in 2019, with EAFSS being a substantial fraction of this output [13]. EAFSS has been successfully used as an aggregate in cement-based materials [18,19], for road pavements [20], and as a non-conventional SCM or filler material for Portland cement (PC) [21–23]. EAFSS, when used as an SCM, has been reported to modify fresh properties such as paste rheology and setting time [21,22,24], albeit with reduced mechanical properties arising from the low reactivity of the EAFSS [25].

Numerous studies have indicated a limited reactivity of both EAFSS and BOFS when used as SCMs. In the case of EAFSS, long setting times were observed even at low replacement levels, leading to decreased compressive strength in blends with typical filler behaviour [26]. A comparison with BOFS as cement replacements reveals that EAFSS exhibits lower reactivity and inferior mechanical properties [26]. Rojas and Sanchez de Rojas [27] concluded that due to its low reactivity, crystalline structure, and stable nature, EAFSS should not be utilised as an active component in cement blends.

Recent advancements in alkali-activation of EAFSS have shown more promising results. It has been demonstrated that EAFSS can be effectively activated with NaOH, but satisfactory mechanical properties are only achieved when blended with fly ash [28]. By utilising a highly concentrated solution of potassium silicate, a compressive strength of 40 MPa can be attained after 90 days [29]. However, the success of the activation process heavily relies on the initial characteristics of the EAFSS. If no cementitious phases or amorphous content is present, the most suitable application for EAFSS would be as a filler or aggregate [30,31].

This study aims to investigate the use of EAFSS as a potential precursor replacement for AAMs, or as a filler material, to reduce the amount of GGBFS required by these mixtures. The fresh, microstructural, and mechanical properties are characterised, along with leachability tests to check the stability of heavy metals in the AAM.

Only limited studies on EAFSS as a partial replacement of known precursors exist, none of which to the authors knowledge report data with replacement levels up to 75 wt%, while achieving high-performance binders. The investigation of EAFSS is necessary as the future of the steelmaking industry transitions to be more reliant on reusing scrap metal, which may completely replace conventional steel manufacture in the future, therefore limiting the supply and availability of current alkali-activation precursors. This work provides a framework for the characterisation and utilisation of alternative metallurgical wastes as high concentration replacements in alkali-activation technology.

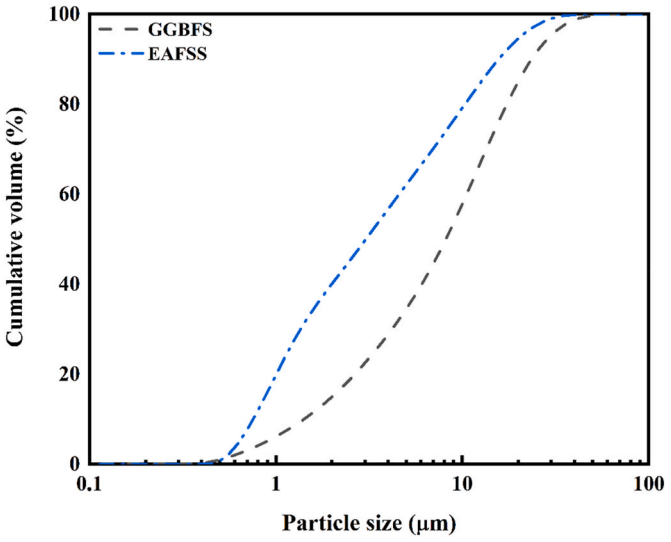

Fig. 1. Particle size distributions of solid precursors used in this study.

It is important to highlight that the present study is part of a broader investigation focused on the use of EAFSS as solid precursors for the production of alkali activated concrete. As such, beyond the findings reported in this article, the authors plan to conduct further research to evaluate the durability and mechanical properties of the resulting alkali activated concrete with EAFSS.

2. Materials and methods

2.1. GGBFS and EAFSS characterisation

In this study, the precursors GGBFS (type eco$_2$cem), with density $\rho = 2.89$ g/cm^3, provided by Ecocem, and EAFSS (type Fillinox 3000, air cooled, subsequently crushed and sieved <100 μm) with $\rho = 3.25$ g/cm^3, provided by Orbix, were used to produce AAMs. The X-ray fluorescence spectroscopy (XRF) results identifying the chemical compositions of the solid precursors are given in Table 1. Apart from the inclusion of Cr_2O_3 in EAFSS, the main distinction between the two precursors is the disparity in concentration of Al_2O_3, MgO, and SO_3. The particle size distributions of the precursor materials are shown in Fig. 1. The GGBFS has d_{90}, d_{50} and d_{10} values of 23.5, 8.0 and 1.4 μm, respectively, compared to 15.6, 3.0 and 0.8 μm respectively for EAFSS. Inspection of the particle morphology via SEM (Fig. 2) shows that the GGBFS particles are more angular, whilst EAFSS particles are more regular with partially rounded edges.

The X-ray diffraction (XRD) patterns of the solid precursors are displayed in Fig. 3. The GGBFS pattern does not show any crystalline peaks. A broad amorphous hump between 25 and 35° 2θ is recognizable. Phase identification of the crystalline phases in the EAFSS XRD pattern indicate the presence of melilite (specifically, åkermanite with partial aluminium substitution, $Ca_2Mg_{0.9}Al_{0.2}Si_{1.9}O_7$, PDF# 04-014-4688), and merwinite ($Ca_3Mg(SiO_4)_2$, PDF# 01-086-6219) as the main mineral

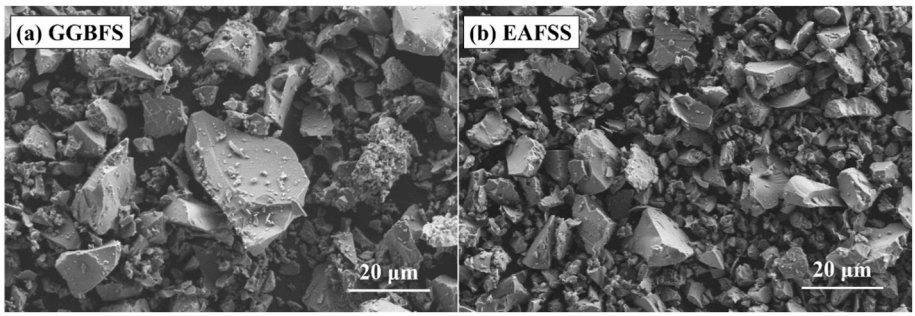

Fig. 2. Morphology of solid precursors by SEM: (a) GGBFS and (b) EAFSS.

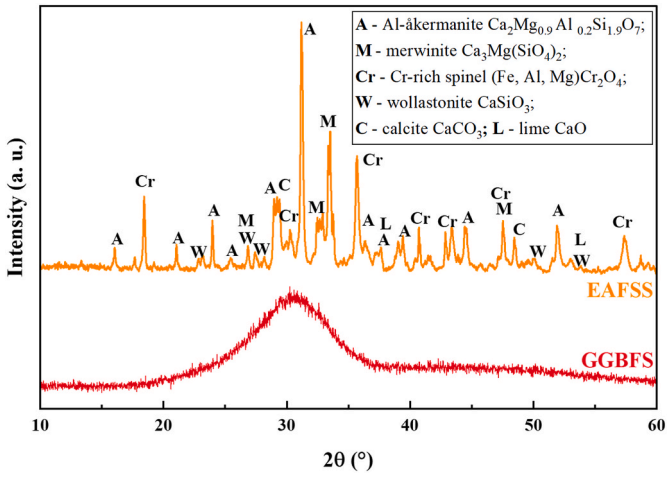

Fig. 3. XRD patterns of GGBFS and EAFSS.

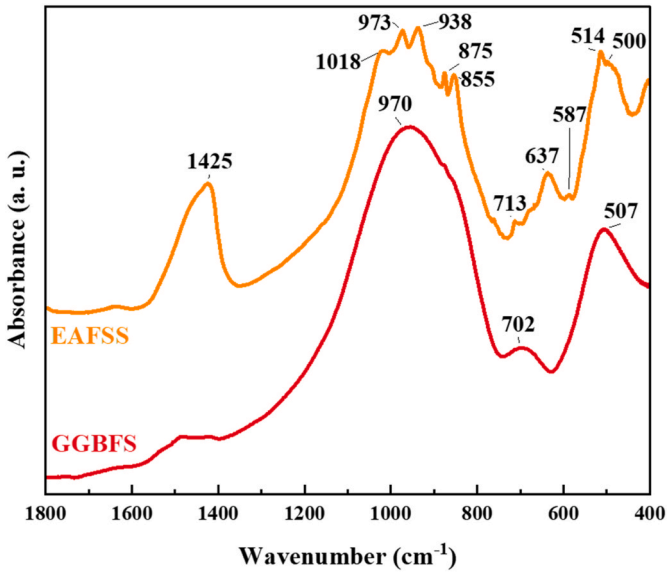

Fig. 4. FTIR spectra of precursors GGBFS and EAFSS.

phases. Less intense peaks corresponding to a mixed spinel phase (Fe, Mg, Al)Cr_2O_4 (PDF# 04-016-2691), calcite ($CaCO_3$, PDF# 01-086-4272), a minor amount of wollastonite ($CaSiO_3$, PDF# 00-027-0088), and traces of free lime (CaO, PDF# 00-037-1497), were identified. The amorphous phase fraction contained in EAFSS is negligible.

The Fourier-transform infrared (FTIR) spectra of the raw materials are presented in Fig. 4. The GGBFS spectrum shows two main absorption bands at ~1000-900 cm^{-1} and at ~500 cm^{-1} corresponding to Si–O-T (T = Si, Al) asymmetric stretching vibrations and Si–O asymmetric bending vibrations, respectively [32]. The broadness of these peaks is indicative of the highly amorphous structure consisting predominantly of silicates.

The EAFSS spectrum similarly exhibits these two main bands, at ~1000-900 cm^{-1} and at ~500 cm^{-1}, corroborating that silicates (calcium silicates with Mg and Al) are the most abundant phases, as seen in the XRD in Fig. 3. Besides these bands, several well defined and sharp peaks are detected for the crystalline phases present. Peaks at 1425 cm^{-1}, 875 cm^{-1}, 713 cm^{-1} are attributed to calcite, specifically the C–O asymmetric stretching vibration and C–O out-of-plane and in-plane bending [33]. The bands at 638 cm^{-1} and the shoulder at 500 cm^{-1} are due to the Cr(III)–O vibration characteristic of the spinel phase (Fe, Mg, Al)Cr_2O_4 [34]. The remnant peaks at 1018 cm^{-1}, 973 cm^{-1}, 938 cm^{-1}, 855 cm^{-1} and 587 cm^{-1} are associated with the presence of crystalline åkermanite, merwinite, and wollastonite [35].

A backscattered electron (BSE) image of a large EAFSS particle with distinct greyscale contrast is shown in Fig. 5. From the energy dispersive X-ray (EDX) elemental map, distinct regions of Cr are observable, which overlap with Mg, Al, and Fe. No Si and Ca are detected within these Cr-rich regions. Primary crystalline phases identified via XRD, åkermanite, and merwinite, have element compositions that include Ca, Si, Mg, and Al, as seen in the bulk of the particle. The calcium silicates åkermanite, merwinite, and wollastonite are known to have low reactivity in alkaline media [36]. Cr containing spinel phases have also been reported in literature, with the Cr occupying the B-site in the spinel AB_2O_4 with an oxidation state of +3. Strong octahedral Cr–O bonding present in the spinel structure is very resistant towards oxidation to the toxic hexavalent state (Cr(VI)) and resistant to dissolution [15]. The leaching of chromium sometimes poses a serious problem for the utilisation of EAFSS in binding materials.

2.2. Activator solution

To activate the solid precursors, a sodium silicate activator was produced by combining sodium hydroxide pellets (Sigma–Aldrich, purity≥ 98%) with a sodium silicate solution, supplied at 45 wt % concentration and a molar ratio SiO_2/Na_2O (MR) of 2.07 (type CRYSTAL 0112, PQ corporation). The alkali solution was prepared 24 h in advance, by mixing sodium hydroxide, sodium silicate, and water to give a molar ratio MR = 1.6 and an activator dose (wt. % of Na_2O with respect to solid precursors) of 5.3 wt %.

2.3. Specimen preparation

Solid precursors (GGBFS and EAFSS) were initially dry mixed in a 2 l capacity Hobart mixer for 60 s to achieve a uniform distribution. Standard CEN sand according to EN 196-1 [37] was also added and pre-blended prior to the alkali-activation of mortars. Both precursors and alkaline solution were mixed for 60 s at low speed (140 rpm), then

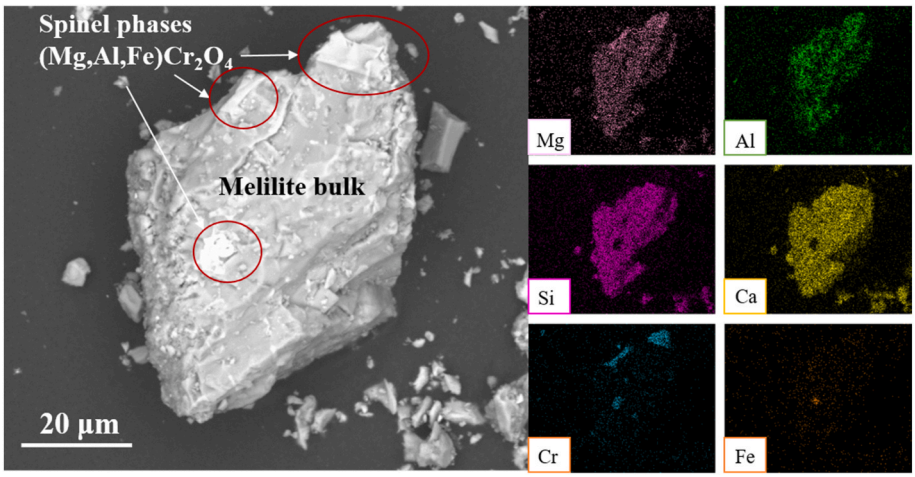

Fig. 5. BSE image of a EAFSS particle with EDS analysis (from top left: Mg, Al, Si, Ca, Cr, and Fe).

Table 2
Mixture proportions of the alkali-activated mixtures.

Mixture	Precursors[a] (g)		Alkaline solution (g)				
	G	E	Sodium silicate	NaOH	Water	w/b	Sand in mortar samples(g)
100G	560.0	0	160	7.7	117.5	0.32	1535.0
25E	420.0	140.0	160	7.7	117.5	0.32	1535.0
50E	280.0	280.0	160	7.7	117.5	0.32	1535.0
75E	140.0	420.0	160	7.7	117.5	0.32	1535.0
100E	0	560.0	160	7.7	117.5	0.32	1535.0

[a] G represents GGBFS, and E represents EAFSS.

subsequently for 90 s at high speed (285 rpm) to achieve a homogeneous mixture. Alkali-activated mixtures were designed with a constant water/binder (w/b) mass ratio of 0.32, where the binder is defined as the sum of the solid precursors plus dissolved solids in the activator. Five slag-based AAMs with varying EAFSS replacement levels (0, 25, 50, 75, 100 wt %) were produced, Table 2.

2.4. Testing programme

2.4.1. Isothermal calorimetry

The heat release throughout the activation process of different alkali-activated pastes was measured with a TAM Air isothermal calorimeter (TA Instruments). To prepare the mixtures, 10 g of solid precursors were weighed and transferred into a glass ampoule. The alkaline solution was added using a pipette and mixed manually for ~30 s. The ampoule was sealed and promptly loaded into the calorimeter which immediately started recording, and this moment is considered the zero in the resulting graph. The heat evolution of the mixture was recorded for 24 h. The results are presented on the basis of the heat release per gram of solid binder, i.e. precursor and solid activators combined.

2.4.2. Ultrasonic pulse velocity

The ultrasonic P-wave of the alkali-activated mortars was measured using a FreshCon system developed at the University of Stuttgart [38–40] for a period of 24 h. Fresh mortar mixtures were poured into a 400 ml U-shaped plastic container at 20 ± 1 °C (RH = 60%) and sealed to avoid water evaporation. A pulsed signal was transmitted every 3 min through the fresh mixture by a broadband piezoelectric transmitter. The resulting signal was received by an ultrasonic receiver and its frequency spectrum analysed to determine the pulse velocity of the fresh mixture, from which both the structural evolution and reaction process were elucidated. The first measurement point in the resulting graph was recorded about 6 min after adding the alkali solution to the dry precursors.

2.4.3. Mini-slump test and setting time

A slump cone with a height of 40 mm, top internal diameter of 38 mm, and bottom internal diameter of 60 mm, was used to determine the workability of the fresh paste as a function of time. For each measurement, the paste mixture was re-mixed manually for 60 s prior to being filled into the slump cone that was placed flat on marked paper. The slump cone was gradually filled, then slowly lifted (<1 cm/s) [41]. The flow spread value was taken as the mean of the slump diameter measured in two perpendicular directions, recorded at 5, 30, and 60 min after the start of mixing.

An automatic Vicat apparatus (Matest VICATRONIC, Impact Test Equipment) was used to determine the initial and final setting times of the fresh pastes following (as closely as possible for alkali-activated pastes) the standard testing procedure EN 196-3 [42]. Fresh pastes were poured into a conical frustum mould with a height of 40 mm, top internal diameter of 60 mm, and bottom internal diameter of 70 mm. The initial setting time was taken as the elapsed time for which the distance between the needle and the base plate was recorded as 6 ± 3 mm, and the final setting time was recorded once a maximum penetration depth of 0.5 mm into the specimen was achieved.

2.4.4. X-ray diffraction

Phase identification and quantification was achieved by analysing X-ray diffraction (XRD) patterns of solid precursors and hardened paste products. XRD patterns were obtained using a PANalytical X'Pert^3 (PANalytical) diffractometer operating in Bragg-Brentano geometry with a Cu Kα radiation source, fitted with a PIXcel-Medipix3 detector. Samples were analysed between the 2θ range of 5–60°, using a step size of 0.02° 2θ. Phase identification was carried out using ICDD PDF+4 (ICDD) and DIFFRAC.EVA (Bruker) programmes.

2.4.5. Fourier-transform infrared spectroscopy

Specimens were prepared by mixing and grinding 2 mg of precursor material with 200 mg of KBr. The mixed powder was transferred to a 13 mm pellet die and pressed to form a transparent pellet. Fourier-transform infrared spectroscopy (FTIR) spectra were collected between 400 and 4000 cm^{-1}, with a resolution of 0.25 cm^{-1}, using a PerkinElmer Frontier FTIR spectrometer (PerkinElmer).

2.4.6. Scanning electron microscopy

Scanning electron microscopy (SEM) images of precursors particles and hardened paste products were obtain using a SEM type TM3030 (Hitachi) coupled with an energy dispersive spectroscopy (EDS) system

Table 3
Heavy metal leaching limits (U1 and U2) established by NEN-7345:94 [45].

	As	Ba	Cd	Co	Cr	Cu	Hg	Mo	Ni	Pb	Sb	Se	V	Zn
U1 (mg/m^2)	40	600	1	25	150	50	0.4	15	50	100	3.5	3	250	200
U2 (mg/m^2)	300	45,000	7.5	200	950	350	3	95	350	800	25	20	1500	1500

QUANTAX 70 (Bruker). Powder samples were prepared by placing a small amount of powder on a carbon dot adhered to a 12.5 mm aluminium SEM pin stub. Loose powder was removed using compressed air. Hardened paste fragments were mounted in epoxy resin, left to cure overnight, and demoulded ready for polishing. Samples were polished using SiC paper in ascending grits and carbon coated prior to SEM analysis.

2.4.7. Mercury intrusion porosimetry

Mercury intrusion porosimetry (MIP) was utilised to study the pore structure of paste specimens after 2 and 28 days of curing. Specimens were immersed in isopropanol for 24 h to halt reaction, then dried in a box oven at 35 °C before being vacuum-dried under 0.1 bar absolute pressure at 20 ± 2 °C for 1 week. Both Pascal 140 (low pressure) and Pascal 440 (high pressure) mercury porosimeters (type Thermo Scientific) were used with a maximum pressure of 200 MPa during measurements to avoid cracking. The contact angle between the mercury and the solid surface was taken as 130° according to Ref. [43].

2.4.8. Strength properties

The compressive and flexural strengths of the alkali-activated mortars were determined from mortar specimens with dimensions 40 mm × 40 mm × 160 mm, according to EN 1015-11 [44], at 1, 3, 7, and 28 days. Specimens were kept sealed in a curing chamber (20 ± 1 °C; 95% relative humidity) until the day of testing. The compressive and flexural strengths for each curing age are reported as the mean value of six (compressive) or three (flexural) measurements performed on the mortar specimens.

2.4.9. Leaching test methodology

The leaching of heavy metals was studied following the procedure described in NEN-7345:94 [45] (tank test), the purpose of which is to determine the leaching of inorganic components from monolithic materials as a function of time, over a period of 91 days of immersion in water. Three cylindrical monoliths were prepared for each composition with diameter of 10 mm and height of 50 mm. Samples were aged for 28 days in sealed conditions to allow stabilisation, and immersed into distilled water in a sealed vessel with a liquid/solid volume ratio of 5. Prior to immersion both bases of the monoliths were sealed with epoxy resin to avoid their contact with water. Extractions of leachate (with replacement) occurred after 1 h, 24 h, then 3, 7, 14, 28, 56, and 91 days in triplicate for each sample. Each leachate was filtered at 0.2 μm, and sent for ICP analysis.

The fraction of leachate (E_i) is calculated as:

$$E_i = \frac{C_i \bullet V}{A} \quad (1)$$

where C_i is the concentration of the component in fraction i, V is the volume of the eluate, and A is the exposed surface area of the specimen, which in this case is the lateral surface are of the cylinder monoliths only.

The cumulative leaching value is then calculated for each component as:

$$\varepsilon_n = \sum_{i=1}^{N} E_i \quad (2)$$

for each of the n elements of potential concern, where N is the number of extractions on time (N = 8 in this case).

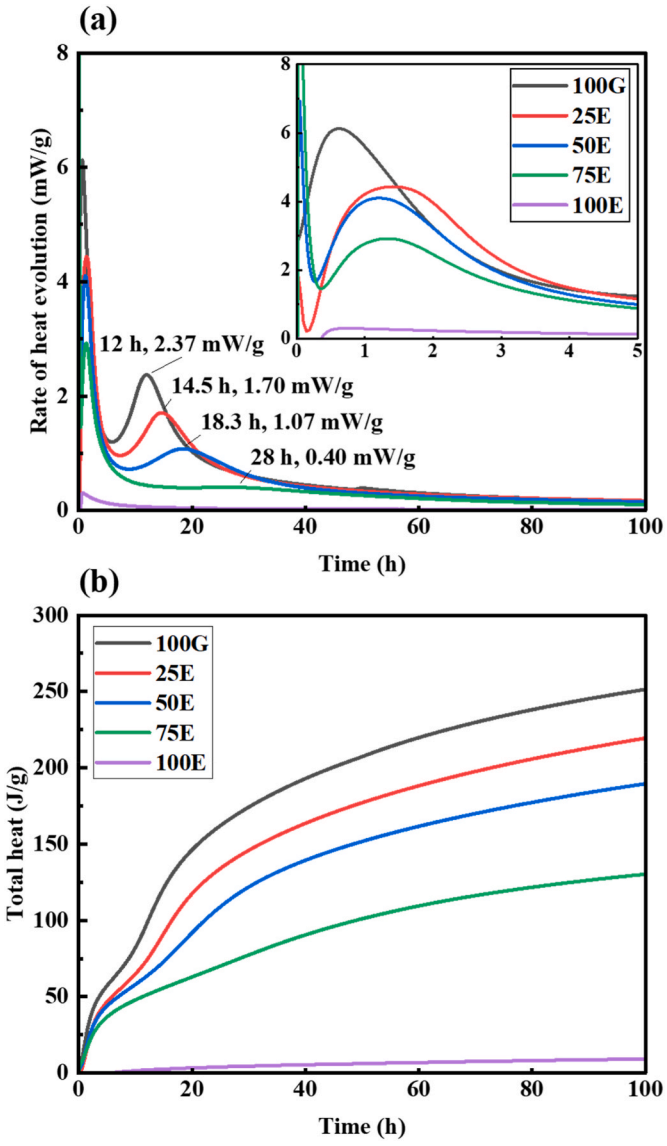

Fig. 6. Isothermal calorimetry data for samples 100G, 25E, 50E, 75E, and 100E, measured at 20 °C.

The materials are classified as a function of cumulative leaching value for each leachate in three following categories according to the limiting concentrations U1 and U2 as shown in Table 3 [45]:

Category 1: ε_n is lower than U1 for each heavy metal present in the sample. These materials do not present any environmental restriction in their use.

Category 2: ε_n is between U1 and U2 for some of the heavy metals present in the sample, but not exceeding U2 for any element. These materials do not face any environmental restriction in their use, but after their service life it is compulsory to remove the contaminant elements with concentrations higher than U1.

Category 3: ε_n is higher than U2 for one or more elements. These materials have a limited utilisation.

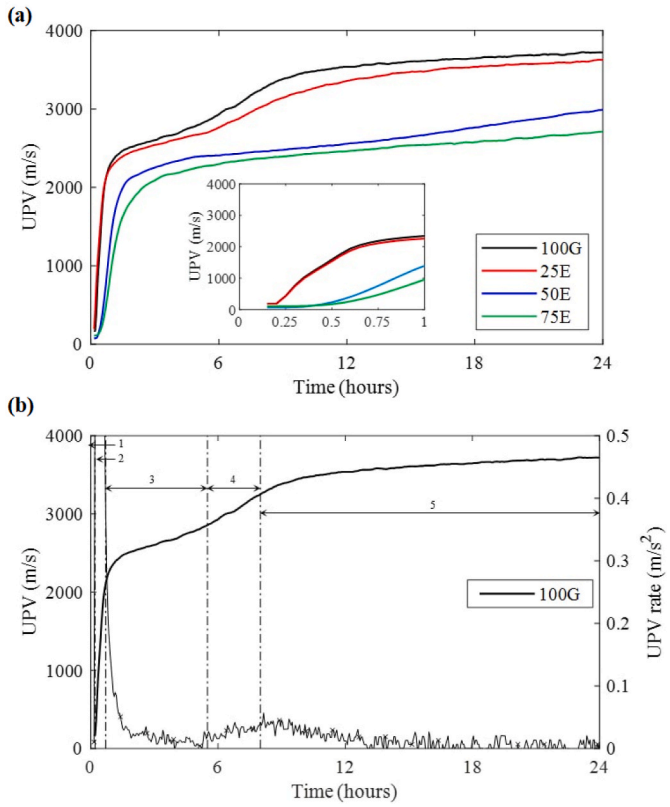

Fig. 7. Structural evolution of alkali-activated mortars in the first 24 h (a) UPV curves and (b) five successive UPV curve stages represented by 100G.

Table 3 shows the values of U1 and U2 for selected relevant elements, according to NEN-7345 [45].

3. Results and discussion

3.1. Isothermal calorimetry

The heat evolution and cumulative heat profiles of the alkali activation reaction of blended GGBFS and EAFSS systems are displayed shown in Fig. 6 (a) and (b), respectively.

One possible classification for the heat evolution of AAMs is into five stages described as: pre-induction or dissolution, induction or dormant, acceleration, deceleration, and the steady stage [46] similarly to traditional cement systems, which is usually acceptable for AAMs activated with sodium silicates. According to this classification we see a first exothermic peak between 0 and 3 h, identified as a pre-induction peak and representing the contact wetting of the solid precursors with the alkaline activator and initial particle dissolution. The formation of primary C-A-S-H and C–N-A-S-H type gels begins with the deceleration of the first peak [47,48]. The intensity of this peak is highest for 100G, decreasing progressively with the addition of EAFSS. For the 100E sample, the pre-induction peak is barely detectable due to the lack of reactivity of EAFSS in this system. The main contribution to the pre-induction peak comes from the ready dissolution of GGBFS particles.

The initial stage of wetting/dissolution of the solid precursors is followed by an induction or dormant period, characterised by a very low, but non-zero rate of heat release in which the dissolution process continues. A second exothermic peak follows the induction period; this is related to the precipitation, nucleation, and growth of reaction products during polycondensation. Within this period a large volume of binding phase, primarily C-A-S-H and C–N-A-S-H type gels, is formed. 100G has an induction period of about 9 h followed by the second exothermic peak, with a maximum at 12 h. Overall, the 100G sample shows an acceleration in heat release and subsequent deceleration within the space of 30 h.

By increasing the replacement level of EAFSS, the induction period becomes longer and there is a reduction in the maximum intensity of the second exothermic peak. This extent of reduction follows a linear relationship ($y = -0.0257x + 2.377$ with $R^2 = 0.994$) with the GGBFS replacement level: reductions of 28.3%, 54.8%, and 83% were observed for 25, 50, and 75 wt% replacements, respectively. This indicates that the reaction of the EAFSS during the acceleration-deceleration period is minimal, and with limited influence from any form of filler effect. 100E mixture has negligible exothermic activity overall.

The cumulative heat is shown in Fig. 6(b). Evaluating the total heat released after 100 h of reaction there is a non-linear trend of heat reduction with the GGBFS replacement (12.7, 24.3, and 48% reduction for 25, 50, and 75 wt% EAFSS, respectively), which indicates that the EAFSS is actually influencing the reaction in these blends to some extent after the initial 20-h period of the main exothermic peaks. However, 100E has a minimal cumulative exothermic activity of 8 J/g after 100 h, which is attributed to the very limited dissolution of particles. These results suggest the low reactivity of EAFSS when included in a blended alkali-activated binder, verifying the potential of EAFSS to be used as a filler material. The cumulative heat release of the blended AAMs from 20 to 100 h may be enhanced by the filler effect of EAFSS which allows a higher space for hydration products and extent of reaction of the remaining GGBFS in these binders.

3.2. Ultrasonic pulse velocity

The evolution of the measured UPV of alkali-activated mortars is presented in Fig. 7. The UPV curve of the AAMs is divided into five successive stages, as shown in Fig. 7 (b) [49]: (1) initial period of very low UPV, (2) first acceleration and (3) deceleration stages, followed by (4) secondary acceleration and (5) deceleration stages. Because the mechanisms (largely physical/microstructural) that cause these stages to occur in the UPV curve are in some way parallel to, and in other ways distinct from the purely chemical that cause the heat release discussed in section 3.1, the comparison between the two techniques can provide further insight into the early-age reaction processes that occur in these cements. A similar trend to that reported by Sun et al. [50] between the UPV evolution and the exothermic process has been found in this study, where the heat flow and cumulative heat evolution can be related to the UPV and UPV rate evolution of the AAMs, respectively.

From Fig. 7 (inset), initial UPV values were measured to be low, which is recognized as the dormant period. These low UPV values are related to the attenuation of ultrasonic waves in early age mortars, induced by interfacial scattering, reflection, and the involvement of air bubbles [39,51].

As the dissolution of solid precursors continuous to takes place, Ca^{2+} cations and other constituents of the GGBFS are released into the pore solution, contributing to the formation of primary C-A-S-H binding gels [52–54] which begin to fill the voids present in the fresh mixture [50]. This accumulation of primary gels causes the ultrasonic wave speed to increase progressively, in stage (2) in Fig. 7, which corresponds to the first exotherm (particle wetting, dissolution, and initial gel formation) in the calorimetry data in Fig. 6(a). Inclusion of EAFSS is seen to delay the start of the increase in UPV, indicating reduced precursor dissolution and reactivity compared to GGBFS, in agreement with previous studies [25,55,56].

With increasing time, the rate of increase of UPV gradually slows as the reaction approaches the first deceleration stage (stage 3 in Fig. 7, corresponding to the deceleration from the first calorimetric peak in Fig. 6 (a). During this stage, the interaction mainly takes place between the cations dissolved from precursor particles and silicate species provided by the activator solution [49]. The UPV growth progressively slowed down, which is associated with a reduction in the dissolution rates of the precursor particles [47,57].

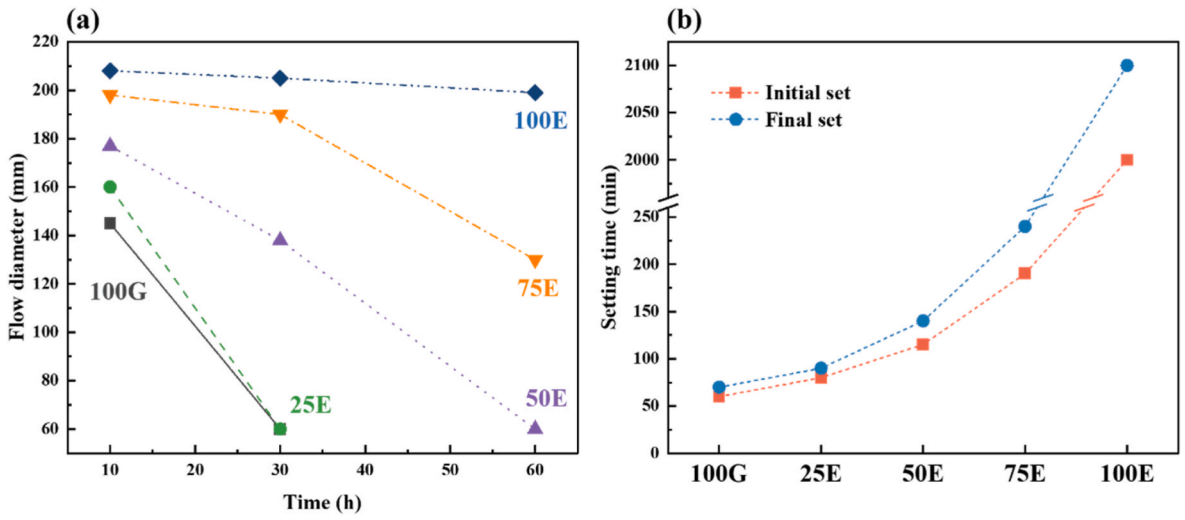

Fig. 8. Fresh properties of the AAMs: (a) flow diameter over time of the GGBFS-EAFSS mixtures; (b) initial and final setting time increasing the replacement level of GGBFS.

A secondary acceleration period is detected at around 6 h (for 100G) and corresponding relatively closely with the onset of the second exothermic in Fig. 6(a). This period is characterised by the involvement of silicate species dissolved from slag particles [49,58] accompanied by the incorporation of aluminate species to form additional C-(N)-A-S-H. The UPV values measured at this stage are sufficiently high to be identified as belonging to a largely-solidified material, and this will be confirmed by the Vicat test results presented below. The secondary rise in UPV is suppressed with increasing EAFSS replacement. Overall, the incorporation of EAFSS retards the structural evolution of the mixtures, as highlighted by the general reduction in maximum UPV. High EAFSS contents are noted to reduce the UPV value significantly within the first 24 h.

3.3. *Fresh properties – mini slump and setting times*

The mini-slump test and setting time results exploring the workability and setting time properties of the tested AAMs are shown in Fig. 8.

As can be seen in Fig. 8 (a), the initial slump diameter values of the paste mixtures with EAFSS vary within the range of 162–212 mm (from an initial cone base diameter of 60 mm), while for the 100G mixture a lower slump diameter value of 149 mm is obtained. Using EAFSS replacement increases the initial slump values of fresh mixtures (9%, 17%, 36% and 43% increase for 25%, 50%, 75% and 100% EAFSS, respectively), despite the higher fineness of the EAFSS. This observation may be attributed to the less reactive nature of EAFSS, consisting of stable mineral phases which do not show pronounced early reactivity [59]. Similar observations have been reported [21,25] where the fresh properties of AAMs improved with different steel slag additions [25,55,56,59] due to their limited participation in early hydration reactions. The larger slump values of the EAFSS fresh mixtures may also be attributed to its higher specific density (Section 2.1) and less angular morphology of particles (Fig. 2) compared to GGBFS. Considering that a constant liquid to solid ratio (by mass) was used to produce the paste mixture, using EAFSS with a higher density than GGBFS yields a larger liquid to solid volume ratio of the fresh mixture, and consequently higher slump values [21].

As demonstrated in Fig. 8 (a), the 100G and 25E paste mixtures showed a drastic loss in the slump values after 30 min, approaching a zero-slump condition (diameter equal to the cone base diameter of 60 mm) at this time due to the intensive early-stage reactions occurring, as illustrated in previous sections. Using higher contents of EAFSS reduces the slope of the slump loss curves, highlighting the retardation of early-stage activation reactions of AAM with increasing EAFSS replacement, in line with isothermal calorimetry and UPV measurements.

The setting time measurements are shown in Fig 8(b). 100G has the shortest initial setting time of 60 min, with final setting measured after 70 min, which is to be expected with the type and dosage of activator used here [60]. Increasing the replacement of GGBFS with EAFSS shows an increase in the initial setting time, by as much as 200% at 75% EAFSS content. A setting time of over 2000 min is observed for 100E.

Comparing Figs. 8(b) and 7, it can be identified that the initial setting times of these specimens appear to correlate quite well with the time at which a UPV of 2000 m/s is reached for the same mortar. This is somewhat higher than values that have been reported for Portland cement-based specimens in the past [39,61]; it remains to be seen whether such behaviour is broadly characteristic of alkali-activated materials as the available data sets comparing UPV and Vicat measurements are very limited.

3.4. *X-ray diffraction*

The XRD patterns of the hardened pastes at 2 and 28 days of curing are shown in Fig. 9. 100G after 2 days (Fig. 9 (a)) shows only one crystalline feature which is attributed to calcite ($CaCO_3$) at ~ 29° 2θ, a product of atmospheric carbonation. Several distinct diffuse humps are detected, at ~29, 33, and 50° 2θ which are related to the formation of C–S–H type gel phases. Only at later ages in Fig. 9(b), two minor humps at ~12° and 56° 2θ are attributed to hydrotalcite-group minerals (approximately $Mg_4Al_2(CO_3)(OH)_{12}\bullet 3H_2O$ PDF #01-089-0460 with variation in Mg/Al ratio and CO_3/OH ratio), resulting from the reaction of the Mg^{2+} present in GGBFS [62]. The broadness and low intensity of these peaks suggests the slow formation of nanoscale hydrotalcite-group crystallites.

When 25 wt% EAFSS is included into the mixture, the crystalline phases åkermanite (A), merwinite (M), and a spinel phase similar to chromite (Cr) are detected, attributed to unreacted EAFSS grains. The formation of C–S–H type gel phases, calcite, and after 28 days, hydrotalcite-group structures is noted, similar to the case of 100G. A further increase of EAFSS content in 50E and 75E causes an increase in intensity of the unreacted crystalline phases, and notably less C–S–H gel formation. Calcite formation is detected, whereas hydrotalcite does not appear to be formed from binder blends with 50% or more EAFSS. When increasing the curing time from 2 to 28 days, an increase in the C–S–H phase fraction is seen, along with narrowing of the C–S–H humps at

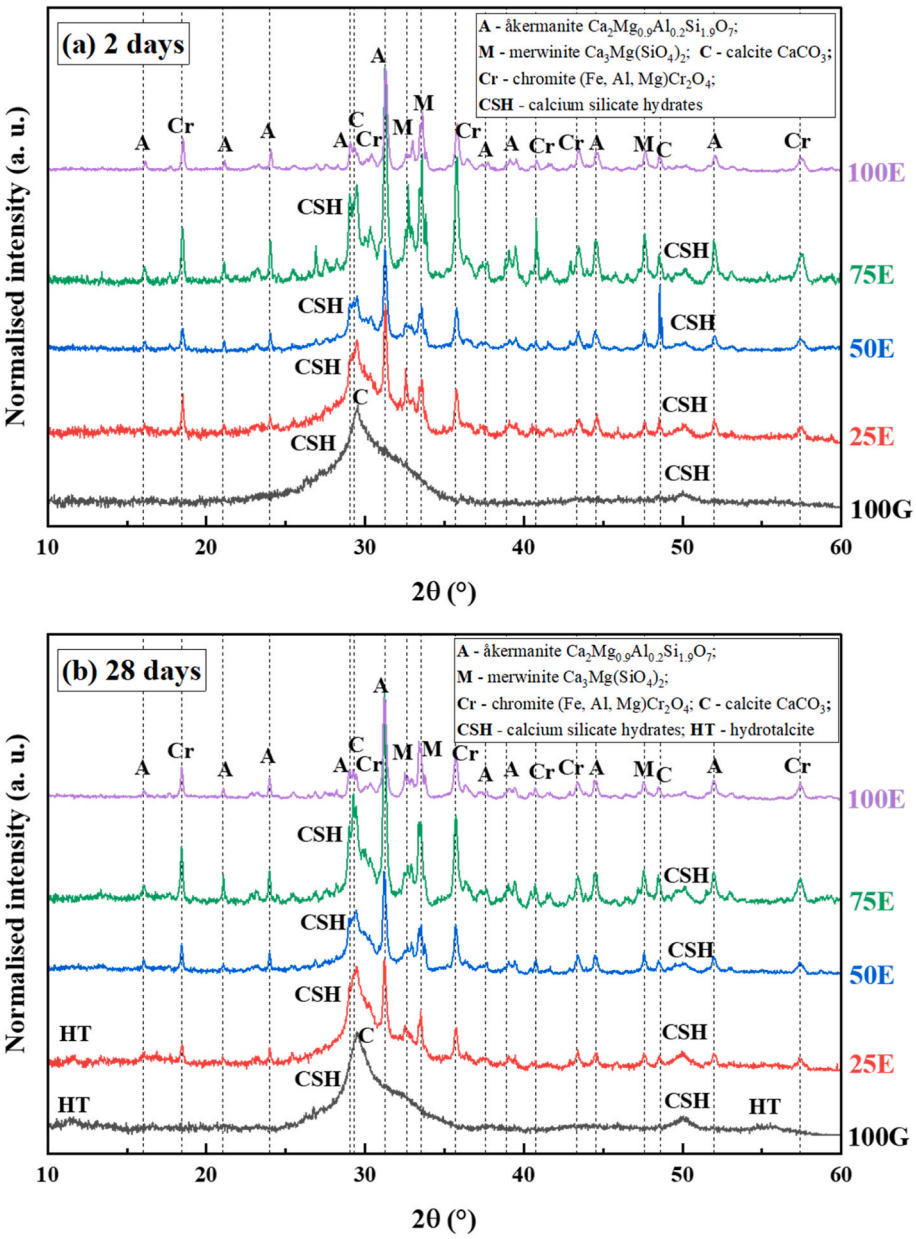

Fig. 9. XRD patterns of AAMs based on GGBFS and EAFSS at 2 and 28 days of curing.

~29° and ~50°, suggesting an increased short-term ordering of the gel [63].The XRD pattern of 100E is similar to that of the EAFSS precursor. C–S–H gel phases do not appear to form, underlining the stability of the crystalline phases present in EAFSS in alkaline conditions.

3.5. Fourier-transform infrared spectroscopy

Infrared spectra of the AAMs cured for 2 and 28 days are represented in Fig. 10. All AAMs studied exhibit absorbance bands at ~3445 cm^{-1}, and 1660 cm^{-1}, which are generally assigned to stretching/bending vibrations of O–H groups. These specific bands are typical of weakly bonded water within the structure, which can occur during the formation of hydration products such as C–S–H type gels. The bands at 1489-1418 cm^{-1} are due to C–O stretching vibrations and can be attributed to atmospheric carbonation products, such as the calcite identified in some samples by XRD (Fig. 9), and also amorphous calcium carbonates [33]. Calcite is also present in the EAFSS prior to activation (Fig. 3), with corresponding absorbance bands at 875-713 cm^{-1} detectable in samples with high contents of EAFSS, such as 100E and 75E.

The main band at 1200-800 cm^{-1} is attributed to asymmetric stretching vibrations of Si–O-T bonds (T = tetrahedral Si, Al) [64]. Analysis of this broad band is used to interpret the chain structure of amorphous gel-type phases present, with a distinct narrowing with increased curing time indicating a shift in structural ordering of the gel phase as the polycondensation reaction progresses [63,65]. This reaction also results in a shift of the band towards lower wavenumbers due to increasing incorporation of tetrahedral aluminium into the silica network [66]. Both of these behaviours are seen to a varying degree in all samples, with slight peak shifts and narrowing of the Si–O-T band with increasing curing time from 2 to 28 days in all samples. It is interesting to note that the 100E sample, which from phase identification of XRD data is believed to be largely unreactive, shows a slight band shift as evidence of partial gel formation, consistent with the low but non-zero calorimetric response of this sample also. This is supported by a relative increase in O–H band intensity from the emergence of hydration products between 2 and 28 days. Sharp peaks at around 1080-940 cm^{-1},

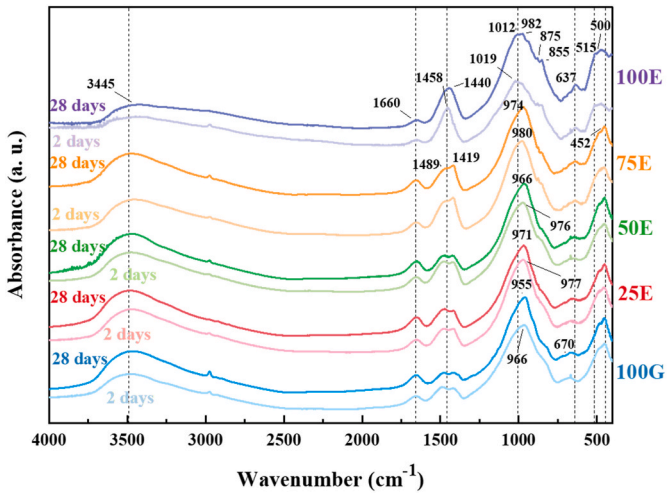

Fig. 10. FTIR spectra of AAMs based on GGBFS and EAFSS at 2 and 28 days of curing.

assigned to åkermanite and merwinite, are more diffuse in character after 28 days, suggesting possible dissolution of calcium magnesium silicate phases and resulting in a weak amorphous gel. Conversely, the bands for the spinel phase (chromite) at 637 cm^{-1} and 500 cm^{-1} remain sharp at all curing times.

3.6. Scanning electron microscopy

Backscattered-electron (BSE) images were collected for 2 and 28-day cured 100G, 50E, and 100E samples. Comparison of Fig. 11 (a) and (b) shows a clear evolution of the 100G binding phase between 2 and 28 days of curing. There is an increase in binding phase present, but also a homogenous distribution of angular GGBFS particles still visible within the matrix after 28 days. Sample porosity is also seen to be reduced with increasing curing time.

In the 50E samples, Fig. 11 (c) and (d), the EAFSS particles can be identified, as well as GGBFS embedded within the binding phase. Some large EAFSS particles show internal greyscale contrast, indicating compositional inhomogeneity. The composition of various EAFSS particles from point EDS analysis (2–5) are shown in Table 4. The GGBFS particles show a reaction rim as they dissolve to form the binding phase, as seen in the 28 day specimen in Fig. 11 (d). The composition of the reaction rim is noted to be different than that of the bulk gel phase, and is consistent with previous observations of hydrotalcite-group phases

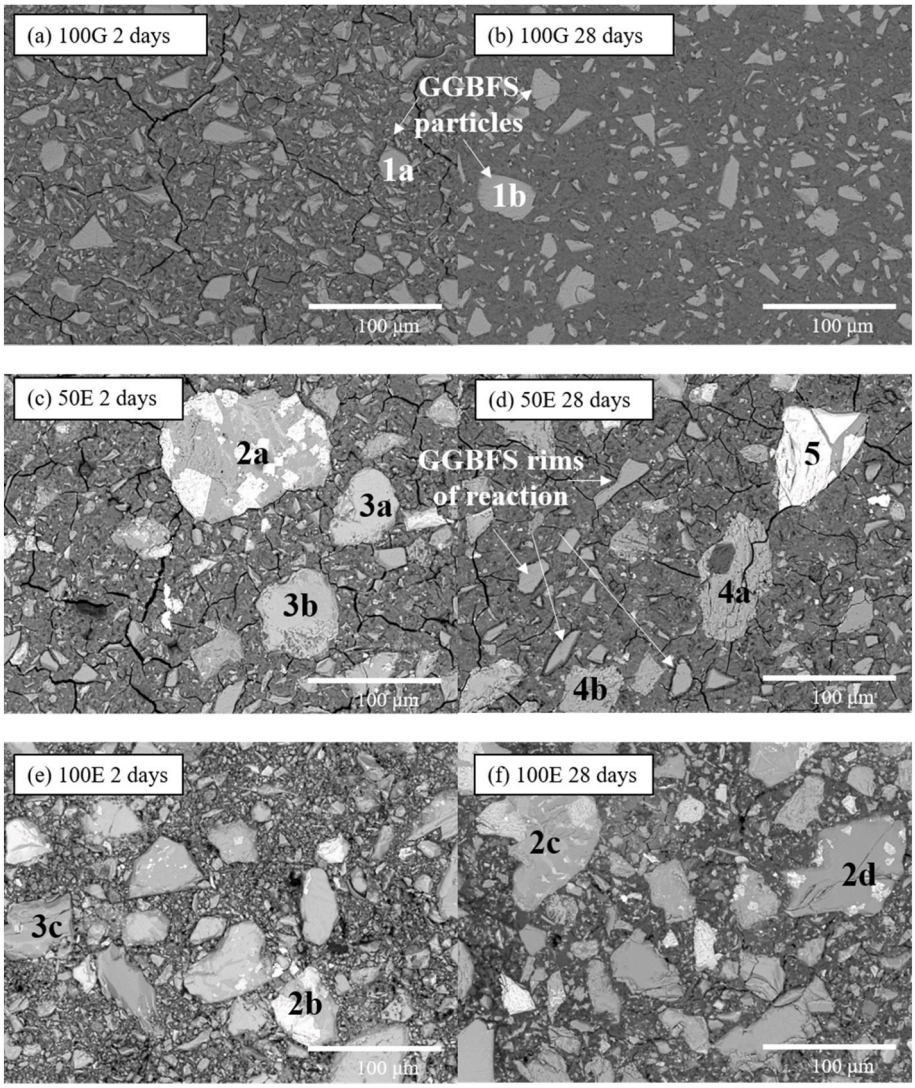

Fig. 11. Backscattered electron images of AAMs based on GGBFS and EAFSS after 2 and 28 days of curing.

Table 4
Compositional EDS analysis of particles of GGBFS and EAFSS labelled 1 to 5 in Fig. 11, where 1 *a* and *b* are GGBFS particles; 2 *a*, *b*, *c*, and *d* are spinel phases embedded in the melilite solid solution; 3 *a*, *b*, and *c* calcium silicates; 4 *a* and *b* are merwinite particles; and particle 5 is an iron silicate.

	GGBFS particles		EAFSS particles									
	Type 1		Type 2				Type 3			Type 4		Type 5
(wt. %)	*a*	*b*	*a*	*b*	*c*	*d*	*a*	*b*	*c*	*a*	*b*	-
O	45.5	46.1	45.7	44.8	47.7	45.0	44.0	43.4	44.9	45.0	42.5	38.3
Ca	27.3	24.6	21.3	28.0	23.0	26.0	36.0	32.8	32.6	27.0	34.1	4.1
Si	17.3	16.8	11.9	13.8	14.0	12.4	15.0	15.3	13.8	11.3	14.1	15.1
Al	5.0	4.9	2.9	1.4	2.8	5.1	1.0	2.6	0.7	0.8	0.5	2.1
Mg	3.5	4.3	3.6	4.3	2.3	3.8	1.7	2.5	5.0	14.1	6.8	0.8
Na	1.2	2.7	1.3	1.1	5.6	0.7	1.8	1.9	1.9	1.1	1.9	4.9
Fe	0.1	0.3	1.3	0.4	0.4	0.2	0	0.1	0	0.5	0.1	34.4
Cr	0	0.1	11.7	5.8	4.6	6.9	0.4	1.3	0.9	0.2	0	0.2

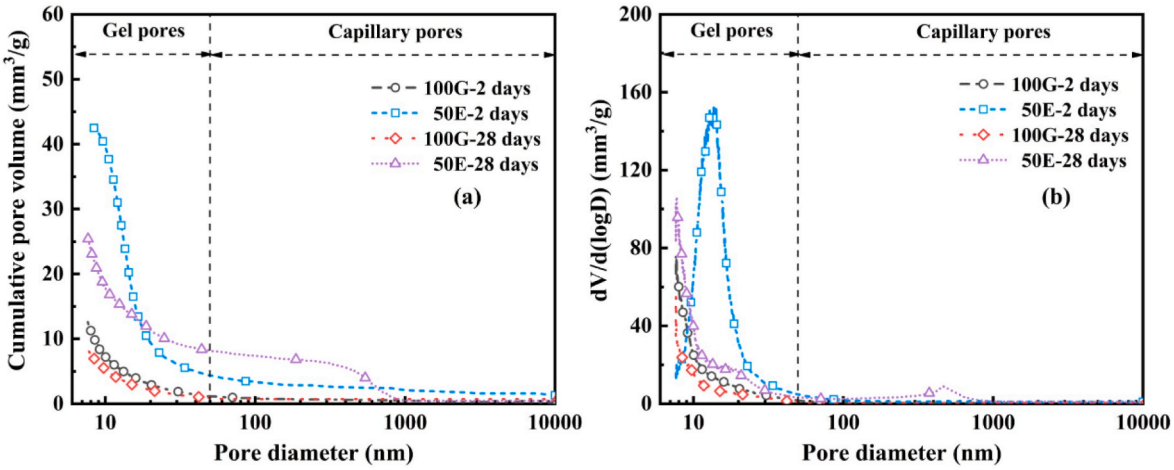

Fig. 12. Pore structure of the alkali-activated pastes after 2 and 28 days: (a) cumulative pore volume and (b) differential pore volume.

becoming formed specifically in this area of the microstructure of alkali-activated BFS-based binders [67]. No reaction rim is seen around EAFSS particles, most likely due to their slower dissolution rate compared to GGBFS.

The 100E sample after 2 day curing in Fig. 11 forms a highly porous matrix with a weak particle assemblage. Curing for 28 days results in an increased binding phase fraction and reduction in matrix porosity, in agreement with the FTIR data (Fig. 10). This confirms that EAFSS in alkali activation can partially form a binding phase from the dissolution of either of the constituent merwinite and åkermanite phases. Engström et al. [36] have previously reported the favourable dissolution of merwinite under alkali activation conditions, and the results presented here are consistent with those findings.

Energy dispersive spectroscopy (EDS) was used to identify several types of particles (labelled in Fig. 11) and to determine their composition, as summarised in Table 4. Particle type 1 is associated with GGBFS, while various EAFSS particles are distinguished: type 2) the spinel (Mg, Fe,Al)Cr_2O_4 embedded in a melilite solid solution phase; type 3) calcium silicate particles with low magnesium content, possibly wollastonite or bredigite ($Ca_7Mg(SiO_4)_4$, which was not clearly detected in the XRD data but could be present; type 4) merwinite particles; and type 5) iron silicate particles, also not identified in the XRD patterns so potentially glassy in nature.

3.7. Mercury intrusion porosimetry

The pore size distributions of 100G and 50E pastes at curing ages of 2 and 28 days, as determined by mercury intrusion porosimetry, are presented in Fig. 12. As reported in the literature [68,69] the pore structure of the AAM matrix can be categorised into three regions: (1) air voids (>10 μm), (2) capillary pores (50 nm - 10 μm) and (3) gel pores (10–50 nm). As shown in Fig. 12 (b), the differential pore volume curves are flattened across the capillary pore region and begin to rise within the gel pore region, indicating that the gel pores are the dominant pores within the paste specimen structure. The shapes of the distributions in Fig. 12(b) show only the 50E mixture having a distinct pore size distribution within the explored range of the MIP test, with the 100G sample possibly containing additional pores <6.5 nm that are not probed by this technique. The total porosities of the alkali-activated pastes in the range of 6.5 nm–10 μm calculated from the total cumulative pore volumes are given in Table 5.

Table 5
Total porosity of the paste specimens in the range of 6.5 nm–10 μm.

Mixture	Total porosity (%)	
	2 days	28 days
100G	2.55	1.75
50E	8.95	5.35

From the data in Fig. 12 and Table 5, blending EAFSS with the GGBFS used to produce AAMs significantly increases the cumulative pore volume of the paste matrix at both ages tested here, yielding a larger total porosity in the range of 6.5 nm–10 μm.

The porous structure of EAFSS pastes arises from the presence of stable crystalline phases that do not participate in the formation of pore-filling gel phases [8,21,25]. The exact nature of the gel type formed in the matrix is also a factor affecting the pore structure of AAMs [70], as each individual type of binding gel promotes a unique pore structure [71].

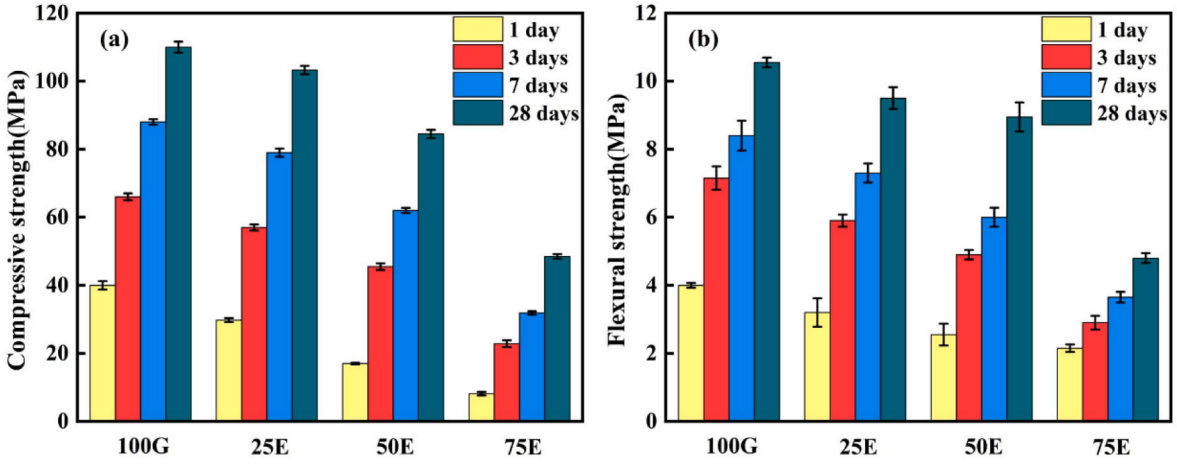

Fig. 13. Strength development of alkali-activated mortars: (a) compressive strength and (b) flexural strength.

Table 6
Results obtained from ICP and calculated following NEN-7345:94 test for samples 100G and 50E, and compared with limit U1.

	As	Ba	Cd	Co	Cr	Cu	Hg	Mo	Ni	Pb	Sb	Se	V	Zn
100G (mg/m^2)	<0.5	3.3	<0.1	0.2	<0.2	<0.2	<0.3	<0.2	2.3	<0.5	<0.8	<1.2	0.2	1.1
50E (mg/m^2)	<0.5	2.1	<0.1	<0.1	<0.2	<0.2	<0.3	13.6	3.3	<0.5	<0.8	<1.2	4.0	1.4
U1 (mg/m^2)	40	600	1	25	150	50	0.4	15	50	100	3.5	3	250	200

As seen in Fig. 12, with continued curing, the total cumulative pore volume of the paste specimens decreases, reflecting the formation of new gel phases filling remnant pores. This is in agreement with studies reporting increasing AAM density with curing age [8,21,72,73].

3.8. Strength properties

The compressive and flexural strengths of the alkali-activated mortars after curing for 1, 3, 7, and 28 days are presented in Fig. 13. Increasing EAFSS replacement results in a reduction in the strength properties of AAMs, consistent with the differences in microstructural evolution and binder densification observed in the preceding sections.

This observation also supports the slower structural development seen in the UPV (Fig. 7) measurements for EAFSS-containing mixtures. The strength properties of mixtures with up to 50 wt% EAFSS replacements are satisfactory for practical applications. The mixtures with 25 wt% and 50 wt% EAFSS showed compressive and flexural strengths that were no worse than 30% below that of 100G. Therefore, incorporation of up to 50 wt % EAFSS can be achieved without major losses in mechanical properties.

3.9. Leaching tests

Table 6 presents the results obtained by ICP analysis of the leachates collected from monolith immersion tests of 100G and 50E. The results are calculated according to NEN-7345:94 [45] and enables the materials to be classified in categories: C1 when the leaching of potentially hazardous elements is less than the limits specified as U1 for each element respectively, C2 when the leaching is between the levels specified as U1 and U2, and C3 when leaching of one or more elements is greater than U2.

All of the values obtained during the leaching tests were below the U1 classification limits for all elements examined, meaning there is no environmental restriction in the usage of these binders according to NEN-7345. Leaching of chromium, which is present in significant quantities in the EAFSS, is not detected from the 50E specimen. This confirms the hypothesis that the chromium present in EAFSS is stable in the solid spinel phase and satisfactorily immobilised within the alkali-activated binder. The presence of a reducing environment within the binders, due to the presence of sulfide from the GGBFS, is also likely to be beneficial in reducing the leaching of redox-sensitive transition metals [74]. The most problematic heavy metal resulting from the test present in EAFSS is molybdenum. The level of 13.6 mg/m^2 is below U1 in the case of 50E, however, it is possible that this element may prove to be a limiting factor on the use of binders with higher EAFSS replacement levels if the U1 value is exceeded and a C2 classification becomes necessary. However, those samples were not able to be tested for leaching within the scope of the current study.

4. Conclusions

The use of EAFSS in blends with GGBFS for producing alkali activated slag-based materials has been evaluated via the characterisation of early hydration and fresh, microstructural, and mechanical properties. Based on this analysis the following main conclusions are made:

1 Replacing GGBFS with EAFSS significantly affects the reaction kinetics, resulting in a significant retarding effect. The dormant period of the heat evolution curve becomes prolonged with higher EAFSS replacements, with a suppression in the secondary exothermic peak after dissolution.
2 The structural formation of the alkali-activated mortars is retarded with increasing EAFSS replacements.
3 EAFSS improved the workability and prolonged the setting time of AAMs due to its lower reactivity compared to GGBFS.
4 The XRD data indicate that most phases of the EAFSS are stable (acting more inert) in alkaline systems, however a small fraction of the EAFSS can react to form a weak binding phase as was observed through FTIR and SEM.
5 EAFSS blending is found to increase the cumulative pore volume of AAMs within the range of 6.5 nm–10 μm, resulting in a more porous structure with coarser pore sizes.
6 EAFSS replacement gives a general reduction in strength properties, although mortars with up to 50 wt % EAFSS exhibit a satisfactory compressive strength after 28 days of 85 MPa, and corresponding flexural strength of 9.5 MPa. This shows that the AAMs produced in

this study fall under the strength class of 52.5 N according to EN 197-1.

7 Leaching tests highlight this GGBFS/EAFSS binder system to be suitable for the immobilisation of heavy metals present within the precursors. All heavy metals detected are well below the U1 limit, meaning that the usage of these binders do not present any environmental restriction (classified as C1). No chromium was detected in the leachates.

Overall, the findings reported in this work can be broadened by upscaling the present formulations to concrete and evaluating the durability and mechanical properties, but also with the comparison to other types of EAFSS.

Declaration of competing interest

The authors declare that they have no known competing financial interests or personal relationships that could have appeared to influence the work reported in this paper.

Data availability

Data will be made available on request.

Acknowledgment

This research study was carried out in the framework of the "By-products for sustainable concrete in the urban environment" (URBCON) project-NWE 725, funded by the Interreg North-West Europe Programme under the EU Cohesion Policy and financed by the European Regional Development Fund (ERDF). Additionally, the authors wish to express their gratitude towards Ecocem, Aurubis and Orbix for providing the GGBS and CS and EAFS used within this study.

References

[1] Y. Ding, J.-G. Dai, C.-J. Shi, Mechanical properties of alkali-activated concrete: a state-of-the-art review, Construct. Build. Mater. 127 (2016) 68–79.
[2] J.L. Provis, Alkali-activated materials, Cement Concr. Res. 114 (2018) 40–48.
[3] J.L. Provis, S.A. Bernal, Geopolymers and related alkali-activated materials, Annu. Rev. Mater. Res. 44 (2014) 299–327.
[4] S.A. Bernal, E.D. Rodríguez, A.P. Kirchheim, J.L. Provis, Management and valorisation of wastes through use in producing alkali-activated cement materials, J. Chem. Tech. Biotech. 91 (9) (2016) 2365–2388.
[5] J.L. Provis, Geopolymers and other alkali activated materials: why, how, and what? Mater. Struct. 47 (1–2) (2014) 11–25.
[6] M. Criado, X. Ke, J.L. Provis, S.A. Bernal, Alternative inorganic binders based on alkali-activated metallurgical slags, in: Sustainable and Nonconventional Construction Materials Using Inorganic Bonded Fiber Composites, Elsevier, 2017, pp. 185–220.
[7] I. Lancellotti, F. Piccolo, K. Traven, M. Češnovar, V. Ducman, C. Leonelli, Alkali activation of metallurgical slags: reactivity, chemical behavior, and environmental assessment, Mater. (Basel) 14 (3) (2021) 639.
[8] R. Cao, B. Li, N. You, Y. Zhang, Z. Zhang, Properties of alkali-activated ground granulated blast furnace slag blended with ferronickel slag, Construct. Build. Mater. 192 (2018) 123–132.
[9] J. Deja, Immobilization of Cr^{6+}, Cd^{2+}, Zn^{2+} and Pb^{2+} in alkali-activated slag binders, Cement Concr. Res. 32 (12) (2002) 1971–1979.
[10] C.F. Pereira, Y. Luna, X. Querol, D. Antenucci, J. Vale, Waste stabilization/solidification of an electric arc furnace dust using fly ash-based geopolymers, Fuel 88 (7) (2009) 1185–1193.
[11] B. Das, S. Prakash, P. Reddy, V.N. Misra, An overview of utilization of slag and sludge from steel industries, Resour. Conserv. Recycl. 50 (1) (2007) 40–57.
[12] Z. Huaiwei, H. Xin, An overview for the utilization of wastes from stainless steel industries, Resour. Conserv. Recycl. 55 (8) (2011) 745–754.
[13] M. Češnovar, K. Traven, B. Horvat, V. Ducman, The potential of ladle slag and electric arc furnace slag use in synthesizing alkali activated materials; the influence of curing on mechanical properties, Materials 12 (7) (2019) 1173.
[14] M. Ozturk, M.B. Bankir, O.S. Bolukbasi, U.K. Sevim, Alkali activation of electric arc furnace slag: mechanical properties and micro analyzes, J. Build. Eng. 21 (2019) 97–105.
[15] W. Li, X. Xue, Effect of cooling regime on phase transformation and chromium enrichment in stainless-steel slag, Ironmak. Steelmak. 46 (7) (2019) 642–648.
[16] Y. Lin, B. Yan, T. Fabritius, Q. Shu, Immobilization of chromium in stainless steel slag using low zinc electric arc furnace dusts, Metall. Mater. Trans. B 51 (2) (2020) 763–775.
[17] H. Zhang, C. Wei, J. Dong, Inhibition kinetics of chromium leaching by calcite coating on the surface of stainless steel slag via the gas–solid accelerated carbonation process, Waste and Biomass Valorizat. 12 (1) (2021) 475–485.
[18] F. Faleschini, M.A. Fernández-Ruíz, M.A. Zanini, K. Brunelli, C. Pellegrino, E. Hernández-Montes, High performance concrete with electric arc furnace slag as aggregate: mechanical and durability properties, Construct. Build. Mater. 101 (2015) 113–121.
[19] S. Monosi, M.L. Ruello, D. Sani, Electric arc furnace slag as natural aggregate replacement in concrete production, Cement Concr. Compos. 66 (2016) 66–72.
[20] M. Pasetto, A. Baliello, G. Giacomello, E. Pasquini, Sustainable solutions for road pavements: a multi-scale characterization of warm mix asphalts containing steel slags, J. Clean. Prod. 166 (2017) 835–843.
[21] W. Song, Z. Zhu, Y. Peng, Y. Wan, X. Xu, S. Pu, S. Song, Y. Wei, Effect of steel slag on fresh, hardened and microstructural properties of high-calcium fly ash based geopolymers at standard curing condition, Construct. Build. Mater. 229 (2019), 116933.
[22] W. Song, Z. Zhu, S. Pu, Y. Wan, W. Huo, S. Song, J. Zhang, K. Yao, L. Hu, Efficient use of steel slag in alkali-activated fly ash-steel slag-ground granulated blast furnace slag ternary blends, Construct. Build. Mater. 259 (2020), 119814.
[23] J. Rosales, F. Agrela, J.L. Díaz-López, M. Cabrera, Alkali-activated stainless steel slag as a cementitious material in the manufacture of self-compacting concrete, Materials 14 (14) (2021) 3945.
[24] E. Furlani, S. Maschio, M. Magnan, E. Aneggi, F. Andreatta, M. Lekka, A. Lanzutti, L. Fedrizzi, Synthesis and characterization of geopolymers containing blends of unprocessed steel slag and metakaolin: the role of slag particle size, Ceram. Int. 44 (5) (2018) 5226–5232.
[25] N. You, B. Li, R. Cao, J. Shi, C. Chen, Y. Zhang, The influence of steel slag and ferronickel slag on the properties of alkali-activated slag mortar, Construct. Build. Mater. 227 (2019), 116614.
[26] F. Saly, L. Guo, R. Ma, C. Gu, W. Sun, Properties of steel slag and stainless steel slag as cement replacement materials: a comparative study, J. Wuhan Univ. Technol.-Materials Sci. Ed. 33 (6) (2018) 1444–1451.
[27] M. Frías Rojas, M. Sánchez de Rojas, Chemical assessment of the electric arc furnace slag as construction material: expansive compounds, Cement Concr. Res. 34 (10) (2004) 1881–1888.
[28] A. Mishra, M. Lahoti, Effect of sodium hydroxide concentration on EAFS based alkali activated binder, Mater. Today: Proc. (2023), https://doi.org/10.1016/j.matpr.2023.03.717 in press.
[29] M. Gómez-Casero, L. Pérez-Villarejo, P. Sánchez-Soto, D. Eliche-Quesada, Comparative study of alkali activated cements based on metallurgical slags, in terms of technological properties developed, Sustain. Chem. Pharm. 29 (2022), 100746.
[30] A. Amani, A.M. Ramezanianpour, M. Palassi, Investigation on the sustainable use of electric arc furnace slag aggregates in eco-friendly alkali-activated low fineness slag concrete as a green construction composite, J. Clean. Prod. 307 (2021), 127257.
[31] S. Kumar, P.K. Gupta, M.A. Iqbal, An experimental study on the development of self-compacting, alkali-activated slag concrete mixes using industrial by-products under ambient curing, Mater. Today: Proc. (2023), https://doi.org/10.1016/j.matpr.2023.04.396 in press.
[32] F. Gervais, A. Blin, D. Massiot, J. Coutures, M. Chopinet, F. Naudin, Infrared reflectivity spectroscopy of silicate glasses, J. Non-Cryst. Solids 89 (3) (1987) 384–401.
[33] L. Addadi, S. Raz, S. Weiner, Taking advantage of disorder: amorphous calcium carbonate and its roles in biomineralization, Adv. Mater. 15 (12) (2003) 959–970.
[34] M. Stefanescu, M. Barbu, T. Vlase, P. Barvinschi, L. Barbu-Tudoran, M. Stoia, Novel low temperature synthesis method for nanocrystalline zinc and magnesium chromites, Thermochim. Acta 526 (1–2) (2011) 130–136.
[35] E.V. Kalinkina, A.M. Kalinkin, W. Forsling, V.N. Makarov, Sorption of atmospheric carbon dioxide and structural changes of Ca and Mg silicate minerals during grinding: I. Diopside, Int. J. Miner. Process. 61 (4) (2001) 273–288.
[36] F. Engström, D. Adolfsson, C. Samuelsson, Å. Sandström, B. Björkman, A study of the solubility of pure slag minerals, Miner. Eng. 41 (2013) 46–52.
[37] EN 196-1, Methods of Testing Cement - Part 1: Determination of Strength, European Committee for Standardization, 2016.
[38] N. Robeyst, E. Gruyaert, C.U. Grosse, N. De Belie, Monitoring the setting of concrete containing blast-furnace slag by measuring the ultrasonic p-wave velocity, Cement Concr. Res. 38 (10) (2008) 1169–1176.
[39] H. Reinhardt, C. Grosse, Continuous monitoring of setting and hardening of mortar and concrete, Construct. Build. Mater. 18 (3) (2004) 145–154.
[40] J. Carette, S. Staquet, Monitoring the setting process of mortars by ultrasonic P and S-wave transmission velocity measurement, Construct. Build. Mater. 94 (2015) 196–208.
[41] J. Gao, A. Fourie, Spread is better: an investigation of the mini-slump test, Miner. Eng. 71 (2015) 120–132.
[42] EN 196-3. Methods of Testing Cement - Part 3, Determination of setting times and soundness, European Committee for Standardization, 2017.
[43] Q. Zeng, K. Li, T. Fen-Chong, P. Dangla, Analysis of pore structure, contact angle and pore entrapment of blended cement pastes from mercury porosimetry data, Cement Concr. Compos. 34 (9) (2012) 1053–1060.
[44] EN 1015-11. Methods of Test for Mortar for Masonry - Determination of Flexural and Compressive Strength of Hardened Mortar, European Committee for Standardization, 2019.

[45] M. Achik, H. Benmoussa, A. Oulmekki, M. Ijjaali, N. El Moudden, A. Touache, G. G. Álvaro, F.G. Rivera, A. Infantes-Molina, D. Eliche-Quesada, Evaluation of technological properties of fired clay bricks containing pyrrhotite ash, Construct. Build. Mater. 269 (2021), 121312.
[46] K.L. Scrivener, A. Nonat, Hydration of cementitious materials, present and future, Cement Concr. Res. 41 (7) (2011) 651–665.
[47] Y. Zuo, G. Ye, Preliminary interpretation of the induction period in hydration of sodium hydroxide/silicate activated slag, Materials 13 (21) (2020) 4796.
[48] C. Shi, R.L. Day, A calorimetric study of early hydration of alkali-slag cements, Cement Concr. Res. 25 (6) (1995) 1333–1346.
[49] R. Cao, S. Zhang, N. Banthia, Y. Zhang, Z. Zhang, Interpreting the early-age reaction process of alkali-activated slag by using combined embedded ultrasonic measurement, thermal analysis, XRD, FTIR and SEM, Compos. B Eng. 186 (2020), 107840.
[50] Y. Sun, S. Ghorbani, X. Dai, G. Ye, G. De Schutter, Evaluation of rheology and strength development of alkali-activated slag with different silicates sources, Cement Concr. Compos. 128 (2022), 104415.
[51] M. Povey, Ultrasonic Techniques for Fluids Characterization, Elsevier, 1997.
[52] D. Krizan, B. Zivanovic, Effects of dosage and modulus of water glass on early hydration of alkali–slag cements, Cement Concr. Res. 32 (8) (2002) 1181–1188.
[53] S. Song, H.M. Jennings, Pore solution chemistry of alkali-activated ground granulated blast-furnace slag, Cement Concr. Res. 29 (2) (1999) 159–170.
[54] M. Palacios, S. Gismera, M.d.M. Alonso, J. d'Espinose de Lacaillerie, B. Lothenbach, A. Favier, C. Brumaud, F. Puertas, Early reactivity of sodium silicate-activated slag pastes and its impact on rheological properties, Cement Concr. Res. 140 (2021), 106302.
[55] Q. Wang, J. Yang, P. Yan, Cementitious properties of super-fine steel slag, Powder Technol. 245 (2013) 35–39.
[56] J. Sun, Z. Chen, Effect of silicate modulus of water glass on the hydration of alkali-activated converter steel slag, J. Therm. Anal. Calorim. 138 (1) (2019) 47–56.
[57] X. Dai, S. Aydın, M.Y. Yardımcı, K. Lesage, G. De Schutter, Effects of activator properties and GGBFS/FA ratio on the structural build-up and rheology of AAC, Cement Concr. Res. 138 (2020), 106253.
[58] F. Puertas, A. Fernández-Jiménez, M. Blanco-Varela, Pore solution in alkali-activated slag cement pastes. Relation to the composition and structure of calcium silicate hydrate, Cement Concr. Res. 34 (1) (2004) 139–148.
[59] M. Salman, Ö. Cizer, Y. Pontikes, R. Snellings, L. Vandewalle, B. Blanpain, K. Van Balen, Cementitious binders from activated stainless steel refining slag and the effect of alkali solutions, J. Hazard Mater. 286 (2015) 211–219.
[60] A. Fernández-Jiménez, F. Puertas, Effect of activator mix on the hydration and strength behaviour of alkali-activated slag cements, Adv. Cement Res. 15 (3) (2003) 129–136.
[61] H. Lee, K. Lee, Y. Kim, H. Yim, D. Bae, Ultrasonic in-situ monitoring of setting process of high-performance concrete, Cement Concr. Res. 34 (4) (2004) 631–640.
[62] M. Ben Haha, B. Lothenbach, G. Le Saout, F. Winnefeld, Influence of slag chemistry on the hydration of alkali-activated blast-furnace slag—Part I: effect of MgO, Cement Concr. Res. 41 (9) (2011) 955–963.
[63] B. Walkley, R. San Nicolas, M.-A. Sani, G.J. Rees, J.V. Hanna, J.S.J. van Deventer, J.L. Provis, Phase evolution of C-(N)-A-S-H/N-A-S-H gel blends investigated via alkali-activation of synthetic calcium aluminosilicate precursors, Cement Concr. Res. 89 (2016) 120–135.
[64] J.A. Gadsden, Infrared Spectra of Minerals and Related Inorganic Compounds, Butterworths, 1975.
[65] S.A. Bernal, J.L. Provis, V. Rose, R. Mejía de Gutierrez, Evolution of binder structure in sodium silicate-activated slag-metakaolin blends, Cement Concr. Compos. 33 (1) (2011) 46–54.
[66] I. García-Lodeiro, A. Fernández-Jiménez, M.T. Blanco, A. Palomo, FTIR study of the sol–gel synthesis of cementitious gels: C–S–H and N–A–S–H, J. Sol. Gel Sci. Technol. 45 (1) (2008) 63–72.
[67] B. Li, Q. Li, W. Chen, Spatial zonation of a hydrotalcite-like phase in the inner product of slag: new insights into the hydration mechanism, Cement Concr. Res. 145 (2021), 106460.
[68] Z. Zhang, L. Li, X. Ma, H. Wang, Compositional, microstructural and mechanical properties of ambient condition cured alkali-activated cement, Construct. Build. Mater. 113 (2016) 237–245.
[69] Y. Ma, J. Hu, G. Ye, The pore structure and permeability of alkali activated fly ash, Fuel 104 (2013) 771–780.
[70] I. Ismail, S.A. Bernal, J.L. Provis, R. San Nicolas, S. Hamdan, J.S.J. van Deventer, Modification of phase evolution in alkali-activated blast furnace slag by the incorporation of fly ash, Cement Concr. Compos. 45 (2014) 125–135.
[71] J.L. Provis, R.J. Myers, C.E. White, V. Rose, J.S.J. van Deventer, X-ray microtomography shows pore structure and tortuosity in alkali-activated binders, Cement Concr. Res. 42 (6) (2012) 855–864.
[72] K. Gao, K.-L. Lin, D. Wang, C.-L. Hwang, H.-S. Shiu, Y.-M. Chang, T.-W. Cheng, Effects SiO_2/Na_2O molar ratio on mechanical properties and the microstructure of nano-SiO_2 metakaolin-based geopolymers, Construct. Build. Mater. 53 (2014) 503–510.
[73] J.S.J. van Deventer, Sindhunata, G. Lukey, H. Xu, Effect of curing temperature and silicate concentration on fly-ash-based geopolymerization, Ind. Eng. Chem. Res. 45 (10) (2006) 3559–3568.
[74] J. Zhang, J.L. Provis, D. Feng, J.S.J. van Deventer, The role of sulfide in the immobilization of Cr (VI) in fly ash geopolymers, Cement Concr. Res. 38 (5) (2008) 681–688.